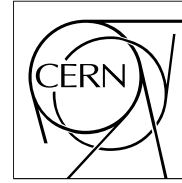**The Compact Muon Solenoid Experiment**

CMS Note

Mailing address: CMS CERN, CH-1211 GENEVA 23, Switzerland

12 April 2001

Readout and Calibration of CMS Pipeline Chips to Examine the Signal Development of Tracking Strip Detectors

M. Petertill, P. Schmitz

RWTH Aachen, III. Physikalisches Institut B, Huyskensweg, D-52074 Aachen, Germany

Abstract

During the last years many investigations have been made to come to an optimal strip detector for the CMS outer tracker, accompanied in the main items by laboratory experiments in Aachen. Prototype testing of MSGCs and a silicon strip detector resulted in a multifaceted VME system with respect to hardware and software. The system includes a DAQ part as well as software tools to check the front end hardware. Results from measurements will be given for the hybrids and the strip detectors. External charge injection and a Sr^{90} source are used to compare the silicon and the MSGC detector.

1 Introduction

In the CMS central tracker $\cong 10^7$ silicon strips will be read out via $\cong 50000$ analogue optical links [1]. Each of the $\cong 80000$ APV front end chips contains 128 charge amplifiers shaping the charge signals with a characteristic time constant of $50\,ns$. An integrated 2-dimensional pipeline capacitor network stores these analogue values every $25\,ns$ in phase with the LHC clock. This method of oversampling the CR-RC pulse allows an analogue pulse shape processor (APSP) to take the linear combination of the stored charges from *three* consecutive bunch crossing intervals (*deconvolution algorithm*). The best set of the three weights (*linear factors*) depends strongly on the detector chosen.

For the CMS silicon microstrip detectors the set of weights has been optimized analytically for the APV6 readout chip ([2], [3]). The optimization ensures a secure bunch crossing identification and simultaneously elimination of pile-up effects at track occupancies occuring in the high luminosity phase of the LHC.

The set of weights for silicon is unsuited for signals from gaseous detectors like the MSGC (or GEM-MSGC) because here each particle track generates several avalanches traversing the $3\,mm$ (or $5\,mm$) detector gap and charge collection is characterized by large fluctuations in size and duration ($45\,ns$—$100\,ns$) which leads to substantial ballistic deficits. Weights can be found therefore only as a compromise between confinement of the signal into a minimum of bunch crossing intervals (BCI) against pile-up sensitivity. To use less than three samples of MSGC pulses was strived for to avoid too many combinations in the track reconstruction programs. For this the APVM readout chip has been designed ([4], [5]). These questions were crucially essential as long as gaseous detectors seemed to be the only affordable solution for the outer tracker.

2 The VME Readout System

Laboratory tests in the construction phase for the final CMS-tracker are quite educational to get a realistic view of the conditions and tasks demanded of the hardware as well as of the software structures. In our present system the algorithms for the digitizer stages – which synchronize and process the analogue data in the counting room – can be freely emulated. The digitizer stages have to interact as a closed system together with the slow control to form a complete DAQ-System.

2.1 Hardware Layout

The DAQ-System has been developed by the authors in Aachen in recent years. Three crates (VME, CAMAC, NIM) are currently placed in one rack as sketched in figure 17. This guarantees modularity and scalability.

A VME *166 MHz* Alpha-CPU (DEC, Compaq) running Digital Unix controls the VME-bus and drives the following modules: a modular number of 4-channel 8-bit VME-FADC cards [7] allowing longword VME access, simple I^2C interface cards for slow control [8] [9] as well as a synchronization unit (RAL Sequencer, [10]) and a port to the CAMAC world. The selection of the trigger source (local/global) and veto times for synchronization purposes are under software control and interlocked by fast NIM logic. As the APV6/APVM need a minimum trigger rate of $\approx$ *100 Hz* for steady operation, we generate a continuous 'background' trigger of this rate. Up to now the delay lines for the sampling phases and the trigger hold-off have to be set manually [1], also the high voltages for the detector supplies.

On the detector side a prototype CMS standard optical readout chain [12] is used for the MSGC and silicon detector setup. The overall bandwidth is bigger than *70 MHz* for the analogue readout chain. Hence signal sampling at *20 MHz* is feasible. The system is plug-in expandable for any reasonable number of the current APV-TRI-Cards [13]. We verified the advantage of optical data links under the noisy electrical conditions in our laboratory where several power supplies are used within the system. Unfortunately we did not manage to have the HV and LV power supplies integrated into a common module [14].

---

[1] a programmable VME variant *PDLU* is under construction [11]

2.2 Software Layout

To avoid unnecessary work we took the L3-tracker online control program named *TAROT*, removed the L3 specific code (avoids rewriting of roughly 15000 lines of code) and implemented the necessary code for the CMS hardware. The program is fully structured, written in Fortran 90 and partially in C++. Main ONLINE features of *TAROT* are [6]:

- language driven
- command logging
- record handler
- cell-wise calibration
- help facility
- error handler
- data compressor
- signal finder

- fully interactive
- macro processor and file execution
- graphics (HIGZ) of data and results
- hardware configuration by files
- foreground–background processing
- slow control by watchdogs
- terminal hardware access
- cluster algorithms

A structured pool of macro commands avoids excessive typing and defines high level commands for calibration, data taking etc. Thus *TAROT* behaves like an object oriented hardware driver with high performance and can be easily adapted to multi processor machines.

3 Judgement of the hybrid quality

When starting a readout system, of course some work has to be invested in procedures like checking for ground loops, common mode noise, good shielding, etc. After that in a first step raw data are taken with program generated triggers (local mode) and displayed online. Several adjustments are performed: shift the offsets of the optical links into their linear region as well as the offsets of the FADC and APV (VADJ) for each analogue channel. All the delay lines have to be tuned. At this stage *TAROT* helps by judging the raw data (figure 1). As can be seen from this figure the digital zero noise is small. The digital one and the tick mark as well as the digital header have the same height. All tick marks have no adjacent signal (correct phase to the *40 MHz* clock). Further data integrity checks concern the following topics: the encoded column address must be valid. It must change at least once within a few triggers. The common mode analogue levels have to stay near their mean values. For offline treatment warning and error flags are recorded within the data records for each trigger and each APV individually.
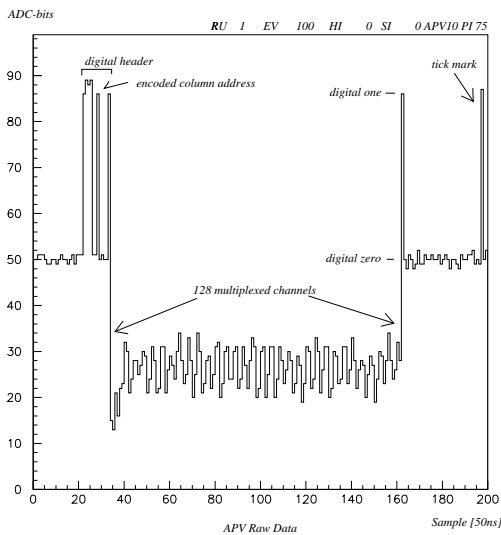
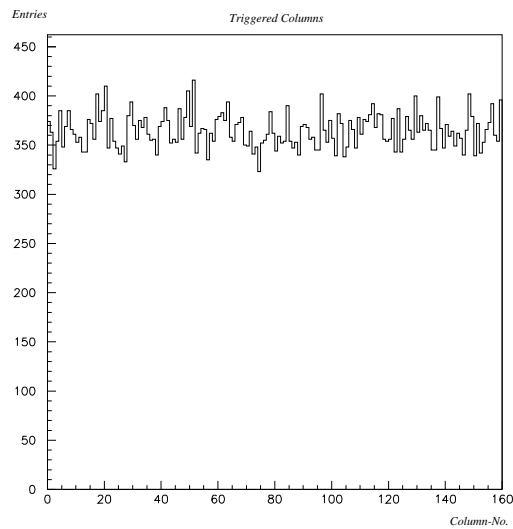

Figure 1: Raw data sample of the APV6

Figure 2: All triggered columns

If not stated explicitly we use the standard parameter set given by the APV6/APVM manuals except for the calibration registers and choose VSHA=50 for the MSGC and VSHA=0 for the silicon detector ([5],[3]) to fix the characteristic time constant correctly.

3

3.1 APV short list

The amount of prototype hybrids×APVs we have tested so far were 1×4, 1×3 of type APV6 and 6×4 of type APVM. Of these 31 two of the seven APV6 and six of the 24 APVM were unusable due to slow control or synchronisation problems. A typical check list concerning these problems can be found in table 5 [15]. I2C register access problems – points 2,3,6,7,11 in table 5 – are examples of slow control faults. Points 8,17,18 of the table can cause synchronisation losses or chip hold-ups. These checks are also included in the *TAROT* error detection part.

3.2 Calibration

Pulse height or clusterwidth distributions rely on a cluster detection algorithm (called signal finder in *TAROT*). Before one can activate such a signal finder the APVs must be calibrated. *TAROT* does this calibration automatically for the following three matrices:

1. pedestal
$$PED\,[i,j] = N^{-1} \cdot \sum_{n=1}^{N} ADCV\,[i,j,n]$$

2. gain
$$GAIN\,[i,j] = N^{-1} \cdot \sum_{n=1}^{N} |ADCV\,[i,j,n] - PED\,[i,j]|_{>5 \times RMS\,[i,j]}$$

3. noise
$$RMS\,[i,j] = N^{-1} \cdot \sqrt{\sum_{n=1}^{N^2} (ADCV\,[i,j,n] - PED\,[i,j])^2]}$$

The matrices of size $i \times j = 128 \times 160$ correspond to the number of channels and the depth of the ring buffer capacitor network (160 columns: $4\,\mu s$). ADCV means analogue to digital converter value. All matrices are created with random local triggers averaging with sufficient statistics the specific quantities offset, gain and noise. Figure 2 shows the number of entries per column after one minute of data taking. They follow a gaussian distribution.

3.3 The matrices

In this section we will show a few examples of the different matrices. The examples were chosen to reveal unusual behaviour.

The internal calibration system of the APV is used to pulse 8 groups of 16 strips sequentially with a programmable charge. The setup of the internal testpulse by means of the registers CDRV, CLVL and CSKW is done with careful attention to the dynamic range of the APV analogue output. Figure 19 shows a normalized gain matrix. To facilitate the optical evaluation of this graph, cells deviating from 1.0 by more than 25 % are set to 1.1. Three columns and one channel turn out to be useless.

During wafer production imperfections often result in high additional cell noise. Figure 20 shows such a frequent case. A wrong synchronization phase easily leads to crosstalk effects; such a case can be seen in figure 21 — pairs of channels always interfere. Of course, in our measurements we have checked and avoided this. Figure 22 displays the RMS-noise matrix of our APV6 hybrid bonded to a silicon wafer [16]. A nearly flat structure with rising noise at the edges is visible. This can be induced by the smallest ground movements.

The individual APV matrices are so characteristic, that they can be used as 'fingerprints' for the APVs. It would be nice to have them in a data base. After bonding the channel defects of the attached sensors are superimposed. An overlap of two to four "dummy" strips at the edges to take account of the rising noise is clearly recommended for safe offline reconstruction.

3.4 The dead cell matrix

By judging the pedestal, gain and noise matrices *TAROT* sets up the dead cell matrices for each individual APV. Dead cell vetoes are used in the signal finder to exclude failure hits in measurements. The effect on data taking in the *TAROT* online analysis and data inspection system will be discussed next, assuming that CMS-like data compression algorithms and signal finding works (p.301 [1]).

Applying the correction for dead cells, as given in the dead cell matrix, takes us from the uncorrected distribution in figure 4 to the distribution in figure 3. In this APVM sample of $\sim 10^4$ random local triggers all fake hits, i.e. readings from dead cells were set to the common mode pedestal value. This correction suppresses mainly the noisy cells shown in figure 23.

After evaluating the calibration matrices we would define three APV6 and 12 APVM as in good condition.
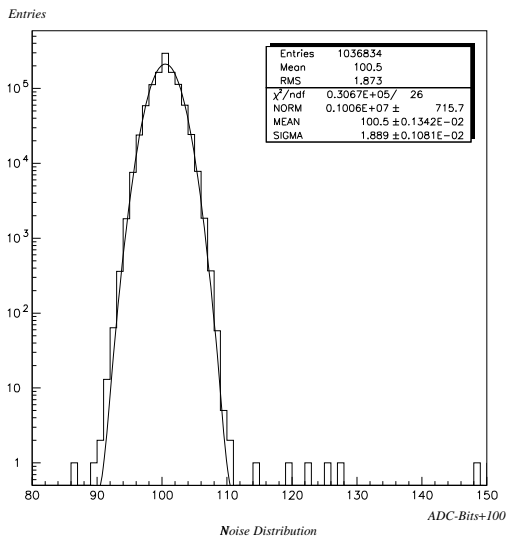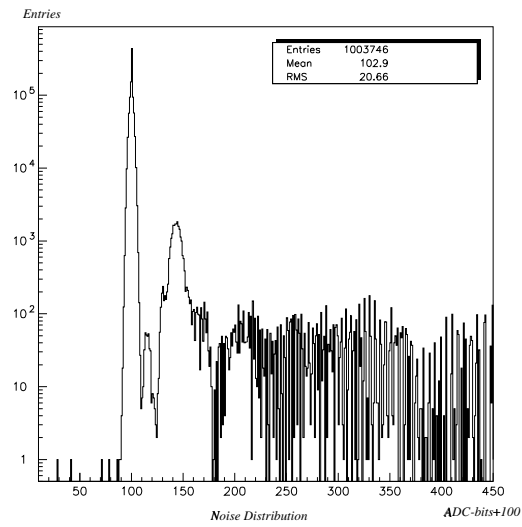
Figure 3: Noise, dead cells excluded

Figure 4: Noise, dead cells included

Noisy cells cannot be completely avoided in production and screening processes, additional cell failures might well occur with increasing radiation doses.

To be on the safe side the column number should be output to the CMS DAQ system (see fig. 5.26, p.301 [1]). This immediately offers the possibility of an online cell based calibration. If in addition one wants to avoid occupancies increasing in time, one should implement a dead cell veto matrix in the Front End Driver (FED, 128×192 bits per APV25).

4   Measurements

In table 1 the most significant sensor parameters are given.

Parameter	Silicon Wafer	MSGC
detector type	FS5KC0-09	MS-9
detector length	$83\,mm$	$100\,mm$
detector width	$109\,mm$	$102\,mm$
detector thickness	$320\,\mu m$	$3\,mm$
detector material	p^+ strips in n-bulk $R_{bulk} = 6\,k\Omega$ crystal orientation $< 100 >$ AC-coupled $C_{AC} \cong 80\,pF$, $R_{poly} \sim 2\,M\Omega$	gold strips on DESAG 263 unpassivated uncoated $Ne/DME = 1/2$
strip pitch	$140\,\mu$	$200\,\mu$
strip-width	$\sim 25\,\mu$	$9\,\mu$ / $70\,\mu$
strip-#	768	512
channels readout	384 by 3 APV6	512 by 4 APVM
trigger window	$1.5\,ns$	$5\,ns$
voltages	$U_{depl} = 100\,V$ / $U_{backplane} = 120..200\,V$	$U_{cathode} = 600\,V$ / $U_{drift} = 2.8\,kV$
currents	$I_{backplane} = 200..300\,nA$	$< 1\,\mu A$

Table 1: Parameters of the sensors tested in the laboratory

5

The (simplified) experimental setup is the following: A Sr^{90} source of $\sim 1\,\mu$Cu and $\sim 2\,mm$ aperture is collimated with a centered tube to a divergence of less than $8°$. The trigger is given by a $10\,mm$ thick scintillator. This leads to a trigger rate of approximately $1\,kHz$ with $2°/_{oo}$ cosmic background.

Interactions of β-particles from the Sr^{90} source with the MSGC material (e.g. drift cathode, glass) are suppressed by a software rejection of multiple hit events, controlled by the clustering algorithms in *TAROT* or the *TARA* offline analysis [17]. This reduces the accepted triggers for MSGCs by 30%.

Note that triggers coming from the scintillators are accepted in windows of 1.5 and $5\,ns$ respectively (around the latency phase). Figures 5 and 6 show typical events seen by the DAQ from these detectors.
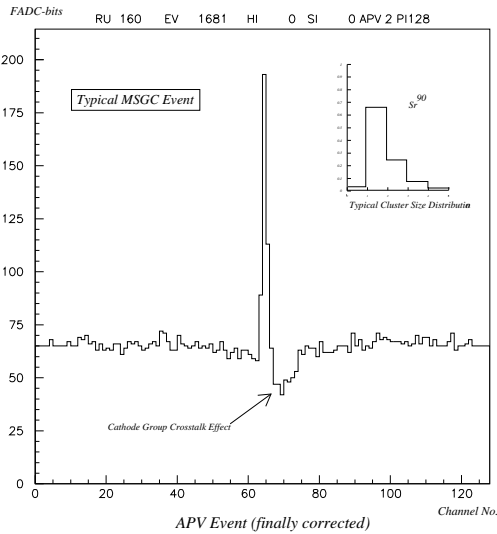
Figure 5: Typical data slice from a MSGC
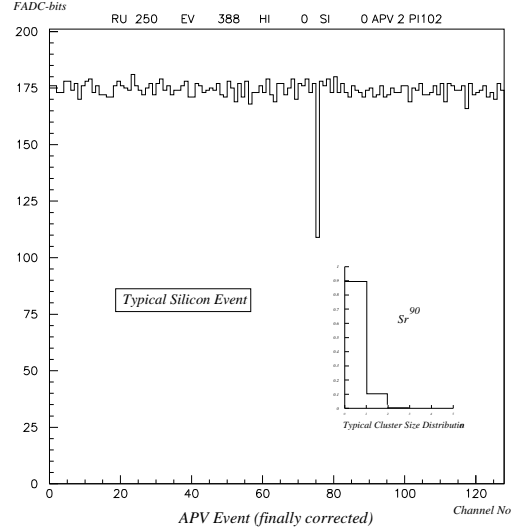
Figure 6: Data slice from a silicon detector

4.1   Tests with injected charges

Well defined charges are injected externally by different techniques into the MSGC or the silicon detector. To examine the signal response of the APV shaper one has to vary the latency (trigger delay) within the time of interest.

Charge injection into a MS9 MSGC is performed via the coupling capacitance between the anodes and the corresponding cathode group of eleven strips. The results of the latency scans in peak and deconvolution mode are plotted in figures 7 and 8 respectively.

One obtains the shape parameters Tau and Alpha ([2], CR-RC$^n \sim (t/\tau)^n e^{-t/\tau}$, $n \Rightarrow \alpha$) by a fit to the data in figure 7. A second fit to the deconvolution data in figure 8 with Tau and Alpha taken from the previous fit, determines the set of weights. Damp is the scaling factor for all weights to set Weight1 to -1.0. Fit results are given by the solid lines.

In case of the silicon detector the charge is injected via a needle probe put on a silicon p^+-strip pad under a microscope. The fitting procedure is identical (figures 9 and 10).

The set of weights for the APV6 is in good agreement with the design values (deviations are less than 3 %). Weight3 of the APVM is 30 % larger than the design value. The main consequence is a bigger undershoot in the deconvolution response (figure 8) behind the zero-crossing at 80 ns.

The shape of the signal is parametrized in the length of the pulse Δt above or below given thresholds measured in % of the maximum or minimum values computed in deconvolution mode (table 2).

The strong bipolarity in the MSGC curve has an impact that cannot be controlled in case of high occupancies. A signal that is two to six bunch crossing intervals earlier in time kills the triggered signal to be measured.
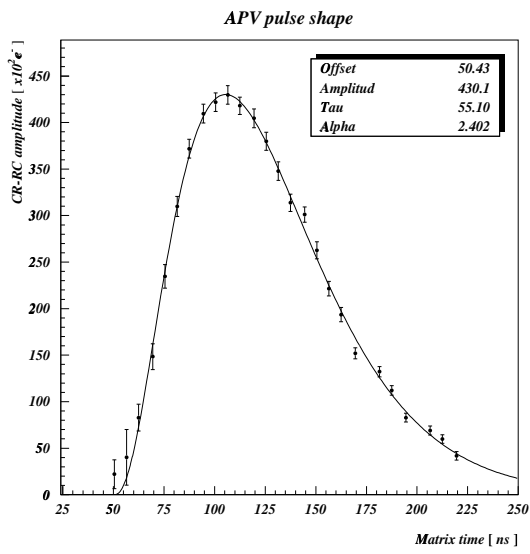
6

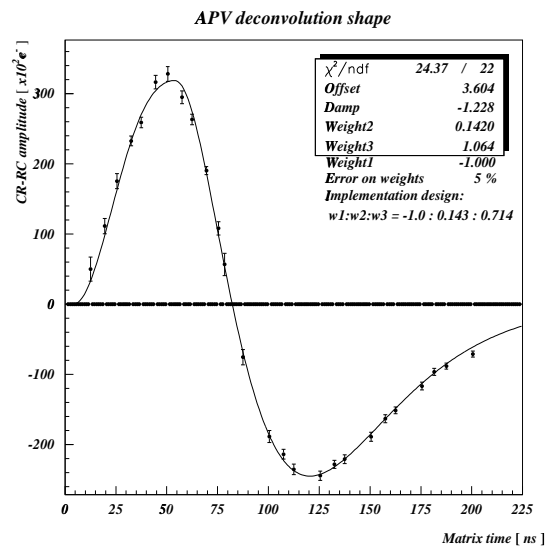**Figure 7:** Pulse shape capacitively injected into an APVM via a MSGC cathode group *)
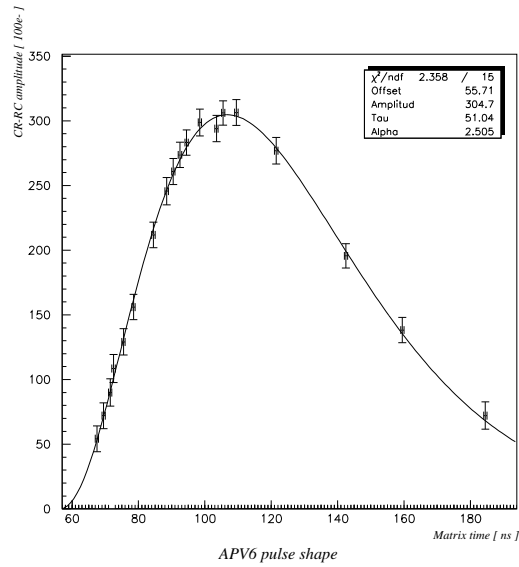

Figure 8: Deconvolution response

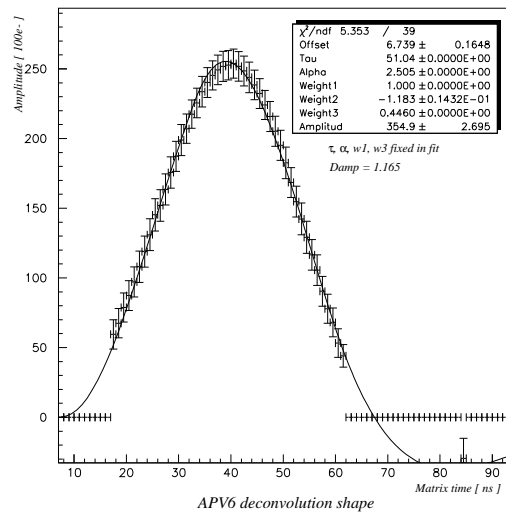**Figure 9:** Pulse shape capacitively injected into an APV6 via a probe on p^+-strip pad

Figure 10: Deconvolution response

	Threshold in % of maximum						$\sim$ minimum	
	95%	90%	FWHM	$1/e$	10%	5%	20%	$1/e$
Δt MSGC $[ns]$	14.3	20.3	46.9	54.2	68.2	71.9	125.0	96.9
Δt Silicon $[ns]$	8.5	11.8	30.2	36.1	49.9	53.5	35.1	30.8

Table 2: Parameterization of the MSGC and the silicon deconvolution signal

---

*) The time scales in figures 7-8/9-10/13-14/15-16 are pairwise identical. By "Matrix time" t_{Matrix} we mean a sum of terms:
$t_{\text{Matrix}} = t_{\text{Region Of Interest}} + t_{\text{Hold Off}} - t_{\text{Latency}}$.

4.2 Sr^{90}-Measurements

Many CMS papers have been published in 1997 leading to the triple set of weights implemented in the APVM. The set of weights was the outcome of a Monte Carlo simulation of an idealized MSGC strip. One important MSGC problem without discussing a special type of MSGC has been described 1998 in reference [18]: It is the mutual inconsistency of "time precision" and "track efficiency" for MSGCs of a given time jitter.

To study the situation in more detail we will compare the MSGC and the silicon detectors showing corresponding figures and tables.

Figure 11 and 12 show typical MSGC and silicon pulse height distributions respectively. Both distributions are obtained at a latency giving the maximum signal over noise in a latency scan in peak mode ('best' Landau). Landau fits are superimposed with the scaling parameters norm NORM, position of maximum MAXP and width SIGMA denoted in the boxes [22].
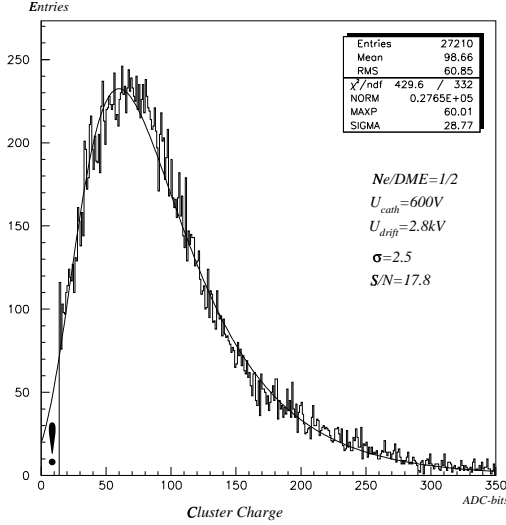

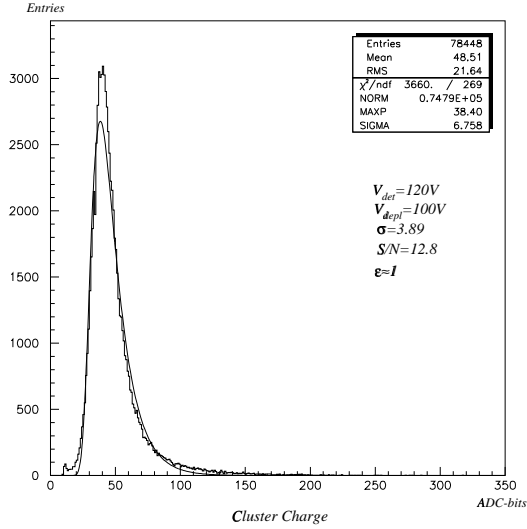| Figure 11: MSGC peak mode Sr^{90} distribution | Figure 12: Silicon peak mode Sr^{90} distribution |

Though the dynamics of the analogue readout is identical, the MSGC pulse height distribution covers 4 times the dynamic range *SIGMA* of our silicon detector while the maximum position *MAXP* is scaling with a factor of 1.6.

The ratio MAXP/SIGMA is ~ 2.5 times greater for the silicon detector than for the MSGC.

This is a mere consequence of the different primary ionizations and their collection or amplification in these detectors. Physical constraints and optimizations for CMS MSGCs and silicon detectors have led to ratios of *MAXP/SIGMA* not differing much from the ones given here. Ballistic deficits in the MSGC case generate a disadvantageous ratio of *MAXP/SIGMA*. The area in figure 11 tagged with an exclamation mark cannot be resolved from the noise.

Now we compare the results of the latency scans for both detectors. To do this we define the expression

$$\text{Acceptability} \; = \; \frac{\text{\# of hits in run}}{\text{\# of triggers in run}} \; \cdot \; \left(\frac{Signal}{Noise} \right)_{\text{mean of run}} \; = \; \epsilon \cdot S/N. \tag{1}$$

In figures 13/14 the peak and deconvolution acceptability scan for the MSGC is shown, in figures 15/16 those for the silicon detector. The error bars arise mainly from the RMS values of the corresponding signal to noise distributions. For a better understanding of these plots the test pulse fits gained in section 4.1 are superimposed as solid lines (the time offsets are fitted individually by eye). To account for ballistic deficits in the *MSGC case* a scale factor of $2/3$ must be introduced to describe roughly the deconvolution amplitude (fig. 14) which is not necessary in the *silicon case*.

A further look at figure 14 confirms a match in polarity and size of the data compared to the deconvolution curve, but the range of acceptability seems very big. Refering to figure 5 clusters are (always) accompanied by induced

charges on neighbouring strips of the cathode group/s hit. Omitting the ground planes on the back side of the substrate and removing some blocking capacitors improves noise performance but at the expense of crosstalk effects (p.197 [1]).

> *Crosstalk effects of the collected charges have been confirmed in our MSGC. As a result*
> *fake hits occur far apart from the plateau, for even more than four bunch crossing intervals.*

In the *silicon detector* a massive external charge injection (sect. 4.1) of >20 mips does not lead to any crosstalk effects. As expected, the analysis of a large statistics of Sr^{90} signals (~ 1 mip) showed no signals of opposite polarity. The corresponding acceptability is presented by star markers in figure 16.

As expected in a jitter free *silicon detector* the acceptability value falls faster than the shaping itself - due to the drop of both factors in the product (1) (figs. 15/16). In the maxima of these scans it reaches a value similar to a Landau signal to noise ($\epsilon \cong 1$). So the acceptability acts as an suitable time and amplitude qualifier for track reconstruction purposes.
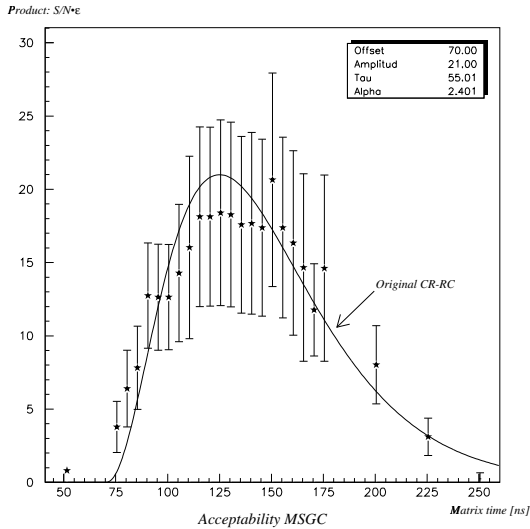

Figure 13: Peak mode acceptability latency scan of the MSGC ($\sigma = 3.5$, energy-cut$= 10$ counts) *)
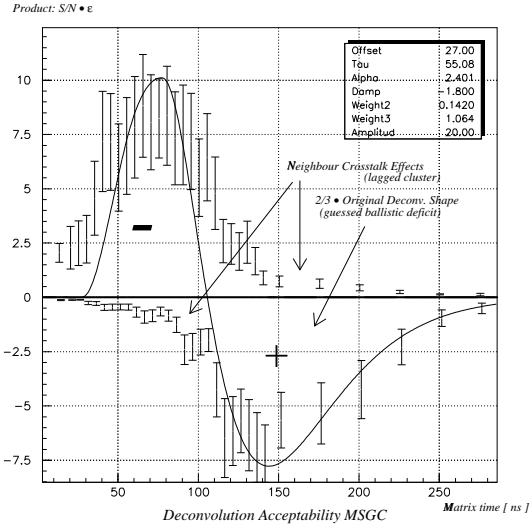

Figure 14: Deconvolution acceptability latency scan of the MSGC ($\sigma = 3.5$, energy-cut$= 10$ counts)
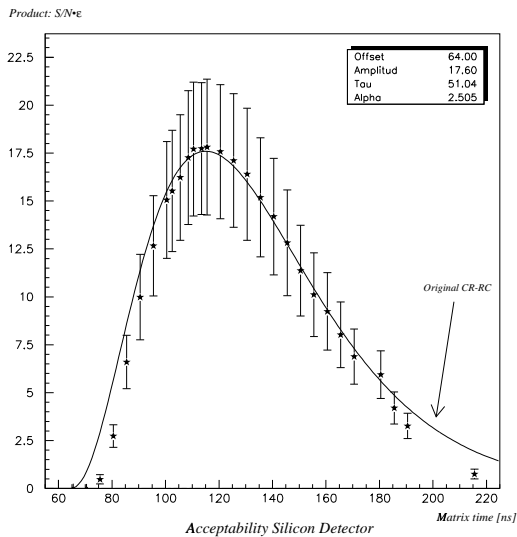

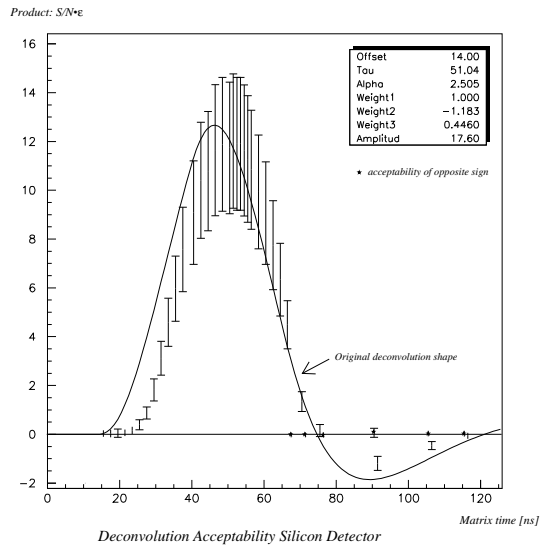Figure 15: Peak mode acceptability latency scan of the silicon detector ($\sigma = 4.6$)

Figure 16: Deconvolution acceptability latency scan of the silicon detector ($\sigma = 4.6$)

detector and APV type	peaking time distance $[ns]$	source
Calibration		
APVM + MS-9	~ 52	fig. 7-8
APV6 + FS5KC0-09	~ 68	fig. 9-10
Strontium 90		
APVM + MS-9	~ 53	fig. 13-14
APV6 + FS5KC0-09	~ 69	fig. 15-16

time window $[ns]$, BCI	sigma cut	acceptability loss [%]
85 , 3.4	53.0	~ 77
90 , 3.6	38.0	~ 61
102 , 4.1	35.0	~ 47
117 , 4.7	29.0	~ 32
150 , 6.0	9.0	~ 6
300 , 12.0	3.5	~ 0

Table 3: Compilation of time intervals between the peaking times

Table 4: Sigma cuts and acceptability losses for given time windows ($\epsilon < 1\%$ outside)

Table 3 summarizes the time intervals between the peaking times of the deconvolution and the CR-RC amplitudes. These times are in good agreement with the deconvolution algorithm. The small deviations from a latency shifted by 50 or $75\,ns$ respectively will be taken care of in the final tracker layout by software adjustable delays in steps of one nanosecond (including the shifts of the sampling points in the digitizer stages).

We now determine the signal degradation in deconvolution mode due to ballistic deficits.

If these are absent as in the *silicon case*, the appropriate noise cut σ separates clearly the 'best' Landau from the noise Gaussian (e.g. $\sigma = 3.89$ in figure 12). In this case any greater noise cut suppresses the hit to trigger ratio ϵ in formula (1) by more than $30\,dB$ outside of a centered time window of $56\,ns$, and by more than $20\,dB$ for a smaller time window of $50\,ns$ (fig. 16).

Next we draw attention to the *MSGC* in deconvolution mode. Looking at figure 14 one sees that the positive acceptability extends over more than twelve BCIs. The relations are given more precisely by the numbers in table 4. Its impossible to define a $30\,dB$ point for the MSGC. This leads to the following result:

Requesting less than 1% of the signals outside an interval of just four bunch crossings
results in a severe loss in acceptability.

The main reasons for this behaviour is the non negligible number of very high pulse amplitudes, the crosstalk effect and the drift time fluctuations typical in MSGCs.

Finally we want to estimate the width of the drift time distribution from the FWHM of the measured deconvolution curve (fig. 14), the calibration fit (fig. 8, tab. 2) and the trigger jitter: $\sim \sqrt{70^2 - 47^2 - 5^2} \sim 55\,ns$. The deviation from the usual $50\,ns$ arises from the change in the gas mixture from *Ne/DME=1/1* to *Ne/DME=1/2*. A drift time of $\sim 45\,ns$ should be achievable with an Ar/CO_2 mixture. This will not significantly change the problems arising from the effects encountered above.

4.3   Comments

A reliable bunch crossing identification is one of the major requirements for a CMS tracking device, among other important features like high rate capability and robustness in a harsh HIP environment. The latter problems seem to be partially solved by the GEM-MSGCs used in HERA-B experiment [20]. An additional GEM amplifier stage [19] allows lower electric field strengths in the transfer gap. The timing property must degrade for the GEM-MSGCs, due to charge depositions in the transfer gap (parallax effect [21]).

Thus a bunch crossing identification within two to three intervals cannot be achieved with a
TDR type MSGC or GEM-MSGC and the proposed deconvolution weights.

Smaller drift time fluctuations are reported from the multi-GEM technology [24]. A special problem for these detectors in combination with a CMOS readout electronics is the wide spread of cluster energies. Saturation effects from high charge depositions may reduce the range of applications. The impact of standard readout algorithms (e.g. discrimination, peak sensing, deconvolution, etc.) remains a field of investigation for these detectors.

5 Conclusions

A prototype MSGC detector and a silicon detector of the CMS outer tracker have been tested with the APV6 and APVM readout chips under comparable conditions. The experience gained by running these CMS pipeline chips in a fully controllable DAQ system have been described in detail. A full cell based calibration shows faulty cells. Their number might grow during the lifetime of the CMS microstrip tracker. Correction algorithms based on a dead cell bit matrix for each APV have been emulated and demonstrated to work successfully.

Measurements with MSGCs of the TDR type show a signal development in excellent agreement with more recent predictions (p.54 [23]) also dealing with triple weight deconvolution algorithms.

The results concerning time development, efficiency and signal to noise ratio for an unirradiated silicon wafer tested in our laboratory are very encouraging for the functionality of CMS.

6 Acknowledgements

References

[1] **CERN/LHCC 98-6 (15-April-1998)**, CMS coll. , *"The Tracker Project Technical Design Report"*

[2] **NIM A320 (1992) pp. 217-227**,
S. Gadomski et al., *"The deconvolution method of fast pulse shaping at hadron colliders"*

[3] **Rutherford Appleton Laboratory (14-Apr-1997)**, M. French, *"APV6 User Manual"*

[4] **CMS IN/1997-021**, F. G. Sciacca,
"Definition of the Front-end Signal Processing Algorithm for MSGCs in CMS"

[5] **APV-MSGC User Guide**, http://www.hep.ph.ic.ac.uk/RD20/msgc_stuff/nffs.html,
Category: New Features: APSP (16-Feb-2000)

[6] **Aachen Reference Manual (May-2000)**, M. Petertill and P. Schmitz,
"TAROT: The APV Read Out Task V8.02"

[7] **Aachen Reference Manual (July-1998)**, F. Beißel, *"VFADC50 V01A"*

[8] **Aachen Reference Manual (June-1997)**, F. Beißel, *"VME - I2C V01A"*

[9] **CERN Reference Manual (June-1997)**, E. Murer, *"VI2C"*

[10] **Rutherford Appleton Laboratory (17-July-1996)**, M. Morrissey, *"SEQSI"*

[11] **A Freely Programmable Trigger And I/O Box (2000+)**, M. Petertill,
"PDLU: Programmable Discriminating and Delaying Logical Unit"

[12] **CERN Reference Manual (August-1999)**,
F. Jensen et al (CME), *"4-Channel Prototype Analogue Optical Data Link"*

[13] **Perugia Project Specification (September-1998)**,
B. Checcucci et al., *"CMS TRI Tracker Readout Interface Board"*

[14] **Recitation at CERN (16-May-2000): http://cmsdoc.cern.ch/Tracker/managment/LHCC/** ,
R. D'Alessandro and G. Parrini, *"General guidelines for the Tracker Power Supply System"*

[15] **http://cmsdoc.cern.ch/cms/cmt/si/ec/cern/www/electronics/electronics.html**,
R. Hammarstrøm, *and follow the link: APVx Chip Distribution pp. 10(15)*

[16] **CMS-T-SSSD43798 Final Inspection Sheet**, Y. Hayama HAMAMATSU PHOTONICS K.K. SOLID STATE DIVISION, *Wafer type FS5KC0-09*

[17] **Aachen Reference Manual (Aug-2000)**, M. Petertill,
"TARA: The APV Readout Analysis"

[18] **CMS IN/1998-015**, G. Hall, *"What is the possible time precision of MSGCs in CMS?"*

[19] **CERN-EP/99-69**, F. Sauli and A. Sharma, *"Micro Pattern Gaseous Detectors"*

[20] **NIM A446 (2000) pp. 324-330**, T. Zeuner, *"The MSGC-GEM Inner Tracker for HERA-B"*

[21] **NIM A443 (2000) pp. 375-385**, T.L. van Vuure et al., *"Properties of the GEM, double GEM and GEM + MGC combination"*

[22] **CERN Program Library 2000**, CERN Computing and Networks Division,
"PAW: Physics Analysis Workstation" [2)]

[23] **CERN/LHCC 2000-016**, CMS TDR 5 Addendum 1, *"Addendum to the CMS Tracker TDR by the CMS Collaboration"*

[24] **NIM A425 (1999) pp. 262-276**, A. Bressan et al., *"Beam tests of the gas electron multiplier"*

IC's	1.	No probe contact
TEST CODES	2.	I2C write error
	3.	I2C read error
	4.	No output enable
	5.	No analogue output
	6.	Stuck bit in I2C register
	7.	I2C read write compare
	8.	Bad currents
	9.	Failed some addresses
	10.	Failed all addresses
	11.	Can't set VADJ
	12.	Some bad pedestals
	13.	Excess bad pedestals
	14.	Noisy analogue output
	15.	Some bad cells
	16.	Channels low calibrate pulse
	17.	Some bad pipeline addresses
	18.	Failed all pipeline addresses

Table 5: A typical check list for APV6/APVM from ref. [15]

[2)] MINUIT Function Minimization: EPS 0.1E-08, ERR 0.5, SEEK $\rightarrow$ SIMPLEX $\rightarrow$ MIGRAD $\rightarrow$ HESSE $\rightarrow$ MINOS
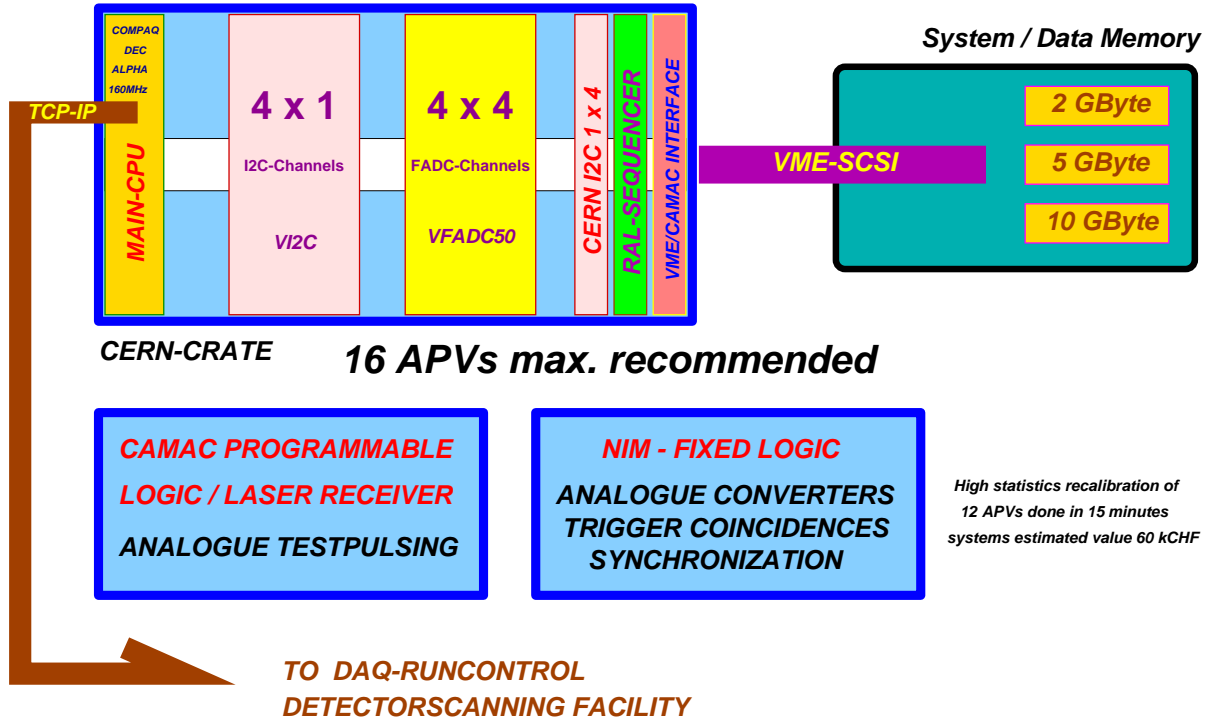
MULTI - MODULE   VME-TESTSTATION

Figure 17: APV DAQ–system, status: 11–may–2000

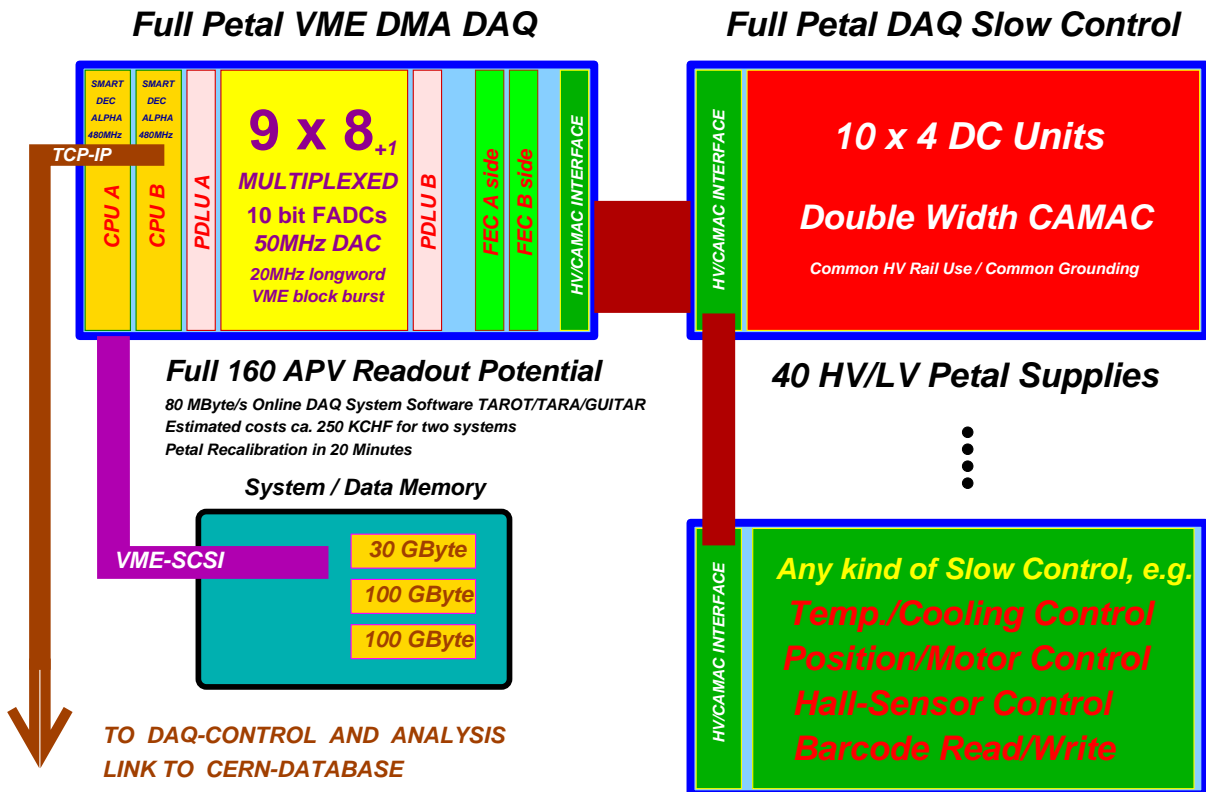*Draft Proposal Lab Petal DAQ, M. Petertill, Aachen May-2000*

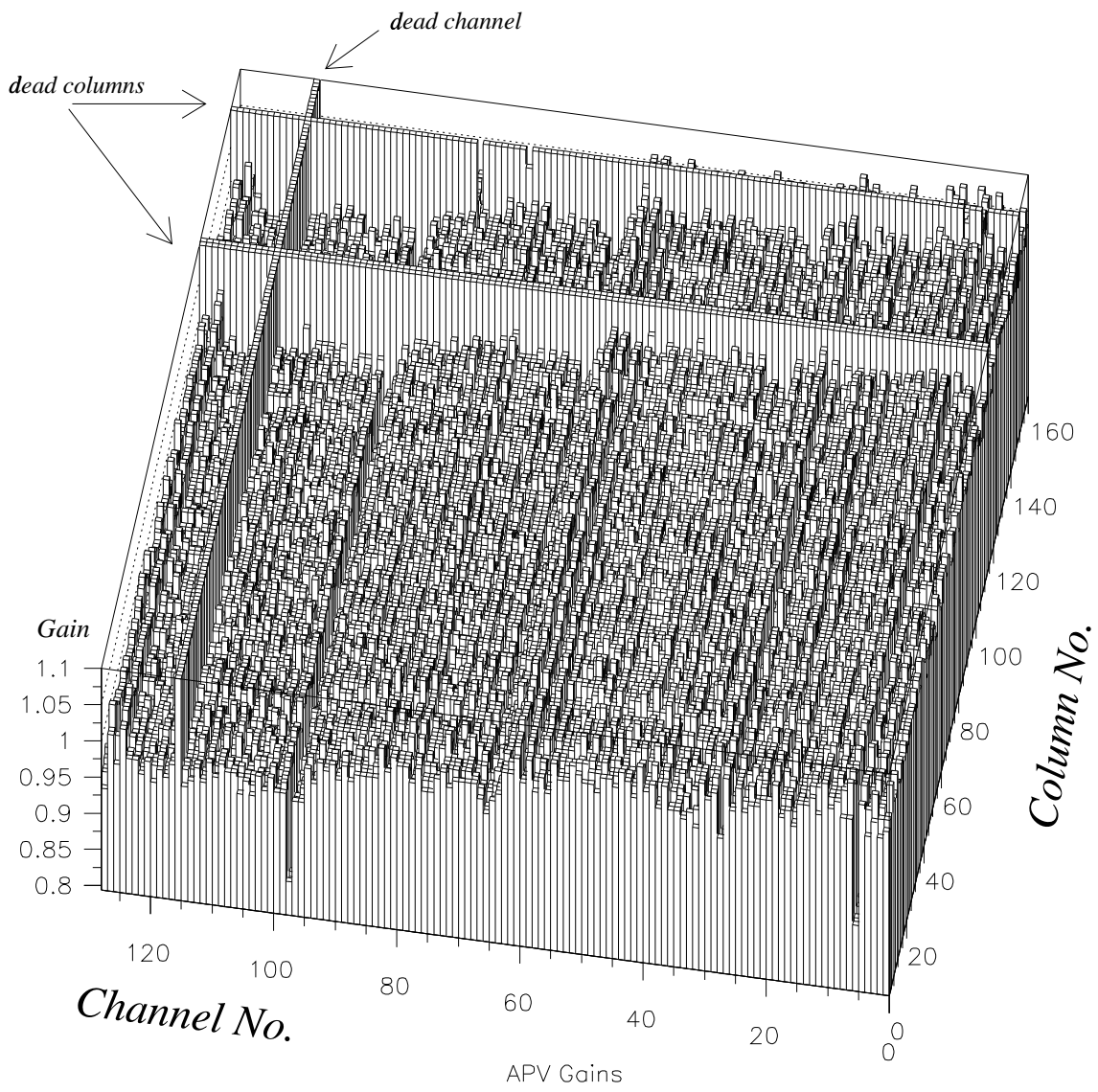Figure 18: Feasibility study of a DAQ upgrade, fig. 17

13

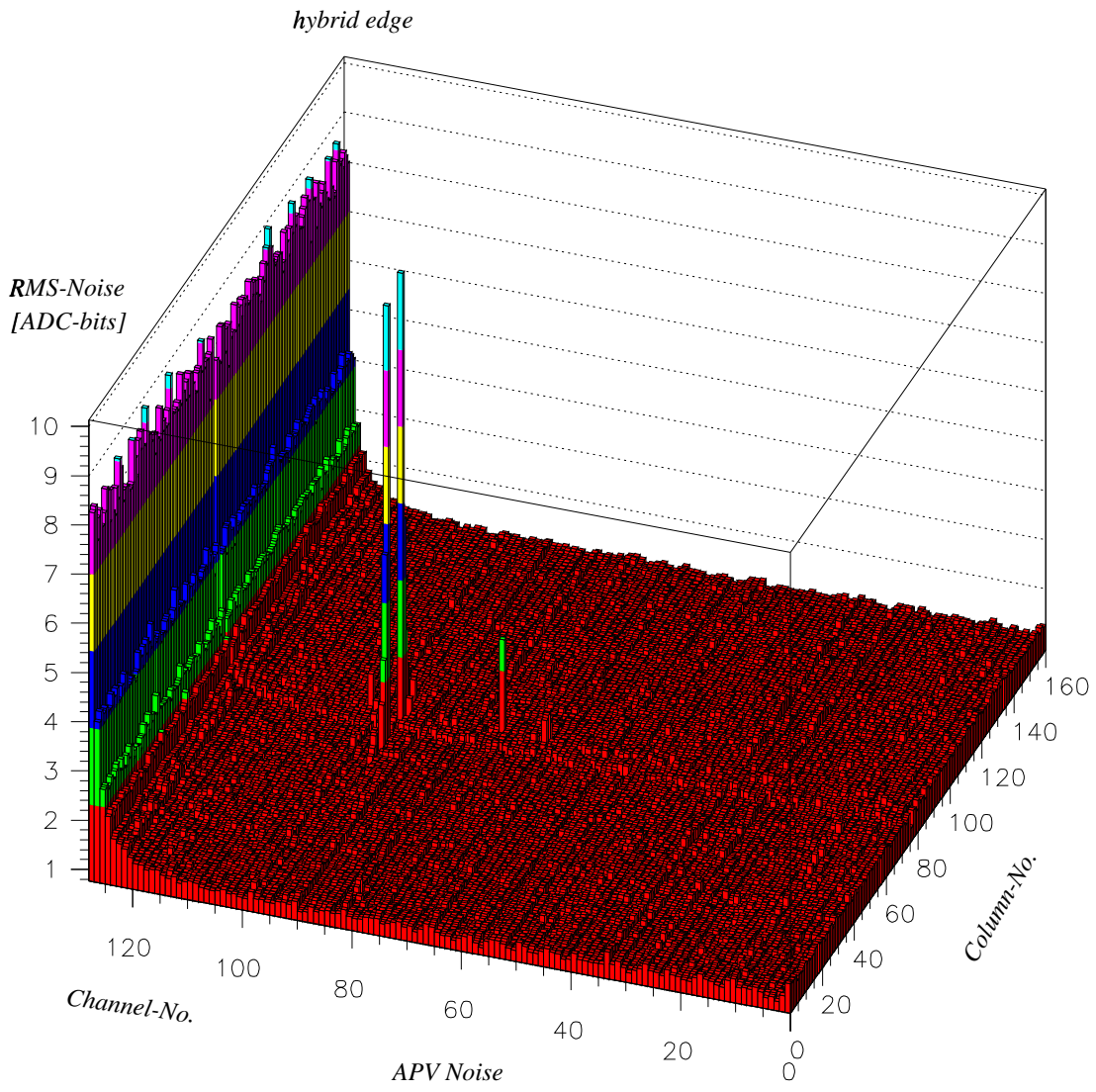Figure 19: Gains of an APV6 received by the internal calibration testpulse system

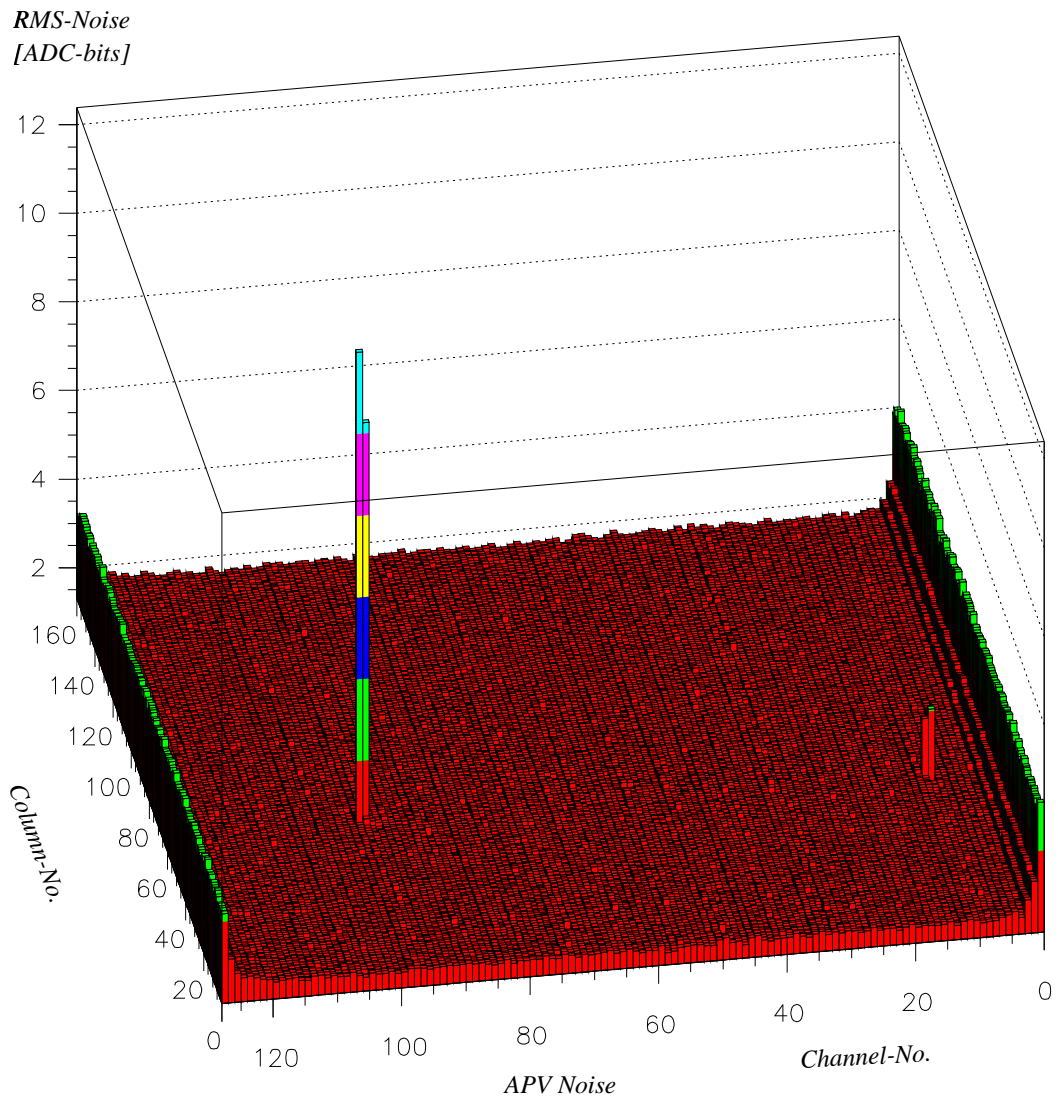Figure 20: RMS-noise of an APVM-hybrid at the hybrid edge

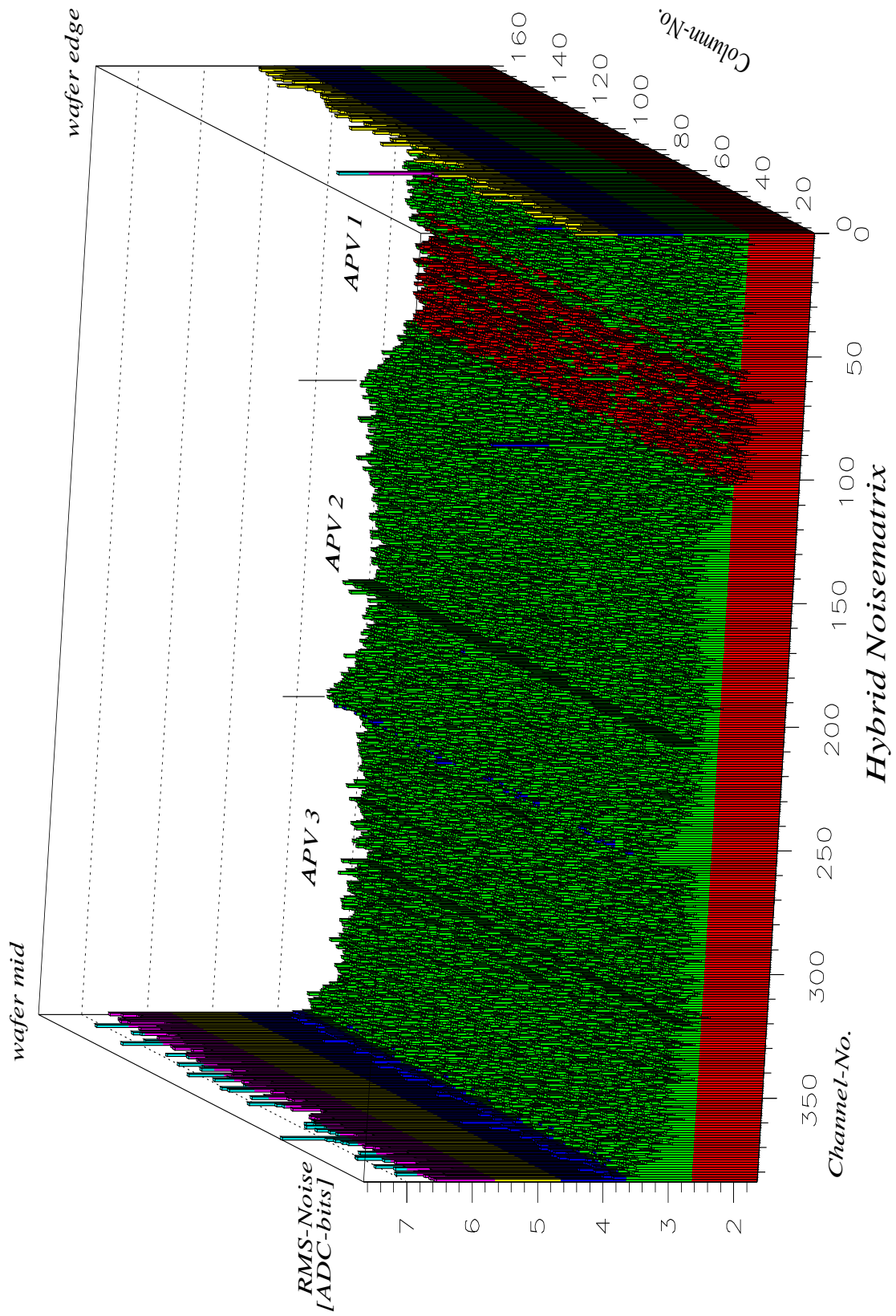Figure 21: Crosstalk of two noisy cells (APVM) caused by a wrong sampling phase

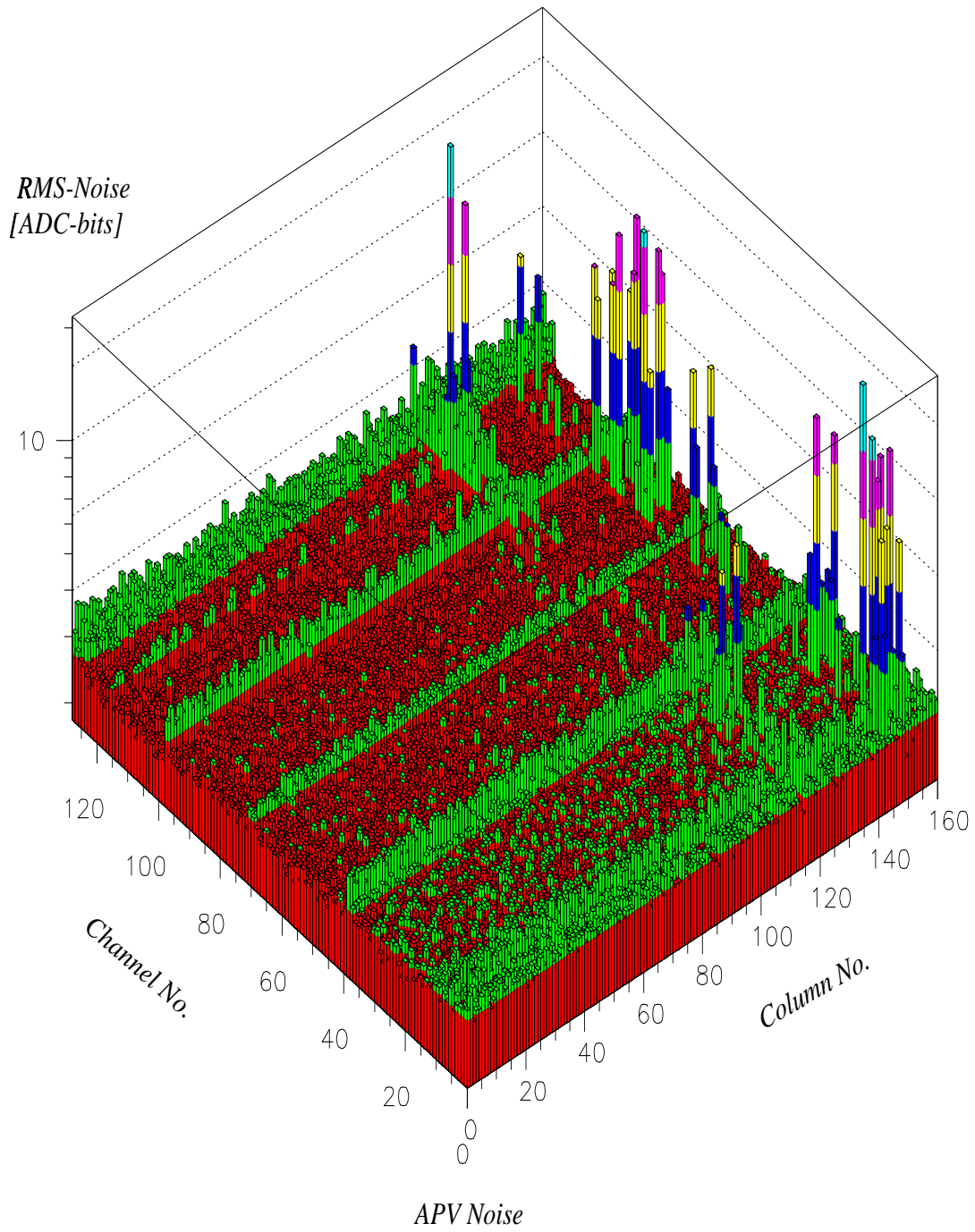Figure 22: RMS-noise of an APV6-hybrid bonded to the silicon detector

Figure 23: Noise matrix of an APVM with circa 30 dead cells